Time-dependent electron-impact scattering from He^+ using variable lattice spacings

M. C. Witthoeft, M. S. Pindzola, and J. Colgan
Department of Physics, Auburn University, Auburn, Alabama 36849
(Received 6 November 2002; published 27 March 2003)

Excitation and ionization cross sections are calculated for e-He^+ scattering at electron impact energies of 100, 200, and 300 eV, using a time-dependent close-coupling method that employs variable lattice spacings. The He^+ ionization cross section is found to be in good agreement with previous converged close-coupling calculations and experimental measurements. Excitation cross sections for $1s \rightarrow ns,np$ transitions in He^+ are presented for high n values well beyond the reach of available experimental measurements and previous nonperturbative theories. The relative difference between the nonperturbative close-coupling and the perturbative distorted-wave results is found to grow larger as the principal quantum number n is increased. This difference has important implications in the collisional-radiative modeling of many astrophysical and laboratory plasmas that use perturbation theory.

DOI: 10.1103/PhysRevA.67.032713 PACS number(s): 34.80.Kw

I. INTRODUCTION

The electron-impact excitation and ionization of low-charged atomic ions at intermediate incident energies remains a formidable theoretical and computational challenge. For all atomic targets, the description of the excitation of bound states near the ionization threshold and the description of the ionization just above threshold must take into account strong correlation effects. In the last few years several nonperturbative theoretical methods have been developed to treat the strong correlation effects found, for example, in the ionization of the neutral hydrogen atom [1–5] and in the excitation of the members of the Li isoelectronic sequence—neutral Li [6], Be^+ [7], B^{2+} [8], C^{3+}, and O^{5+} [9].

In this paper we calculate excitation and ionization cross sections, using a time-dependent close-coupling (TDCC) method [3] that employs variable lattice spacings. The main limitation for the TDCC and other nonperturbative methods is the size of the numerical region in which all the Coulomb interactions are treated exactly. For the ionization just above threshold, and for the excitation of bound states with high principal quantum number n, the numerical box size needed becomes quite large. Variable lattice spacings allow the numerical box size to increase without a concurrent increase in the overall computational run time. A time honored method in atomic structure calculations is to either double the step size of the radial distance r at regular intervals [10], or to transform to a new variable $\rho = f(r)$. Two popular choices have been $\rho = \sqrt{r}$ and $\rho = \ln(r)$. On the other hand, for atomic collision calculations it is also important to limit the largest step size in the radial distance r so that a suitable representation of high momentum continuum states can be retained. Thus, in this paper we do not transform to a new variable ρ, but employ a variable lattice spacing with both a minimum and a maximum radial step size.

We test our formulation of the TDCC method with variable lattice spacings by examining electron scattering on He^+. The total ionization cross section for He^+ has been experimentally measured by Peart *et al.* [11] and Defrance *et al.* [12] and has been calculated by using the convergent close-coupling [13] and R-matrix B-spline [14] methods. Excitation cross sections for the transitions $1s \rightarrow ns,np$ ($n = 2,3,4$) have also been calculated by using the convergent close-coupling method [15]. The remainder of the paper is organized as follows. In Sec. II we use the variational principle to derive a discretized Hamiltonian operator for a continually changing nonuniform mesh. In Sec. III we examine the dangers of a doubling mesh when applied to electron scattering from a model He^+ ion. In Sec. IV we apply the TDCC method with a continuously changing nonuniform mesh to calculate excitation and ionization cross sections for e-He^+ scattering. Finally, in Sec. V, we give a brief summary of our findings on the strength of correlation effects in e-He^+ scattering. Unless otherwise noted, atomic units are used throughout this paper.

II. VARIATIONAL PRINCIPLE

A numerical representation of the time-dependent radial Schrödinger equation for a single electron in the field of a nucleus is derived from the variational form [16]

$$\frac{\delta}{\delta P^*(r,t)}\left(i\int_0^\infty P^*(r,t)\frac{\partial P(r,t)}{\partial t}dr - \frac{1}{2}\int_0^\infty \left|\frac{\partial P(r,t)}{\partial r}\right|^2 dr - \int_0^\infty P^*(r,t)V(r)P(r,t)dr \right) = 0, \tag{1}$$

where $P(r,t)$ is the reduced radial wave function and $V(r) = l(l+1)/2r^2 - Z/r$. If we represent the derivatives and integrals with low-order finite differences, discretizing space on a uniform mesh yields

$$i\frac{\partial P_j(t)}{\partial t} = (HP)_j(t)\ , \tag{2}$$

where the Hamiltonian operator is given by

$$(HP)_j(t) = -\frac{1}{2}\left(\frac{P_{j+1}(t) + P_{j-1}(t) - 2P_j(t)}{h^2} \right) + V_j P_j(t), \tag{3}$$

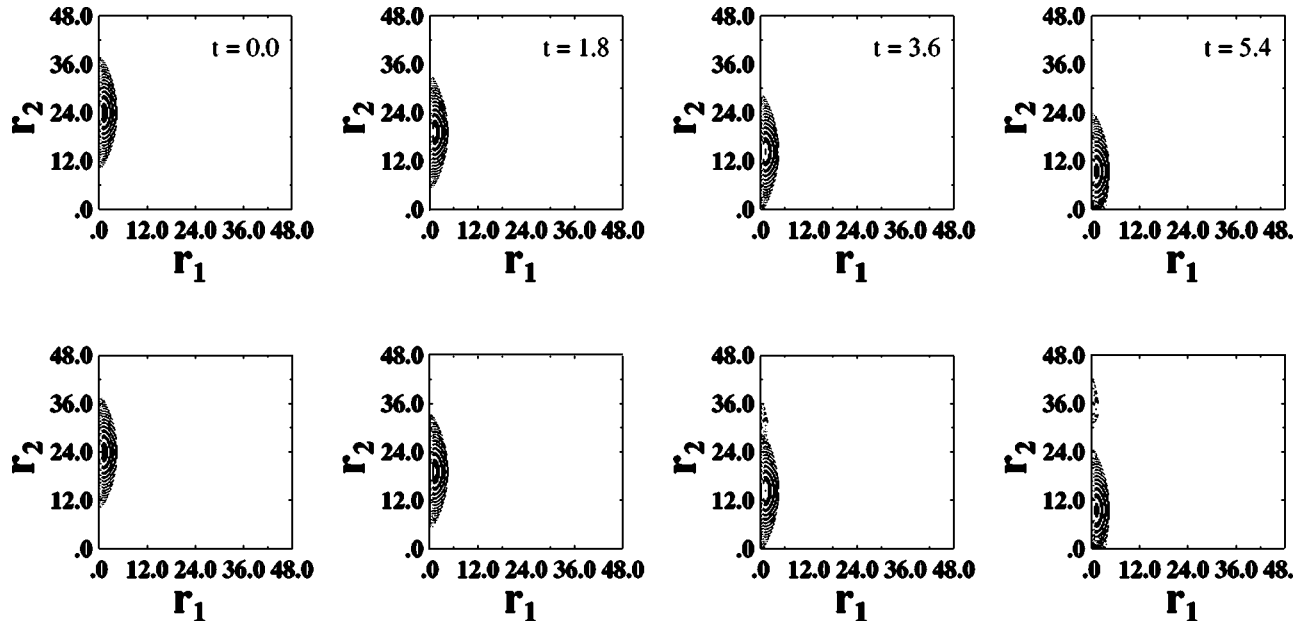

FIG. 1. Probability density $|P_{ss}(r_1,r_2,t)|^2$ at $E=100$ eV, using a fixed mesh (top row) and a doubling mesh (bottom row) for various times during the early phase of scattering (radial distances are in atomic units, 1 a.u.$=5.29\times10^{-9}$ cm; time is in atomic units, 1 a.u. $=2.419\times10^{-17}$s).

and h is the uniform mesh interval. On the other hand, discretizing space on a continually changing nonuniform mesh yields a Hamiltonian operator given by

$$(HP)_j(t)=-\left(\frac{P_{j+1}(t)}{h_j(h_j+\bar{h}_j)}+\frac{P_{j-1}(t)}{\bar{h}_j(h_j+\bar{h}_j)}-\frac{P_j(t)}{h_j\bar{h}_j}\right)+V_jP_j(t), \tag{4}$$

where $h_j=r_{j+1}-r_j$ and $\bar{h}_j=r_j-r_{j-1}$. The discretization of Eq. (2) in time, for either a uniform or a nonuniform spatial mesh, using the staggered leap frog method [3] yields

$$P_j(t+\Delta t)=-2i\Delta t(HP)_j(t)+P_j(t-\Delta t), \tag{5}$$

where Δt is the time interval. Norm conservation is exact if we adjust Δt to be smaller than the smallest $(h_j)^2$ on the spatial mesh. A power series expansion of the time evolution operator, e^{-iHt}, around $t=0$ provides a way of initializing the two-step algorithm of Eq. (5).

For many purposes it is quite useful to generate a complete set of bound and continuum orbitals by direct diagonalization of the one-electron radial Hamiltonian matrix. For a uniform mesh the H matrix is symmetric, while for a nonuniform mesh the H matrix is nonsymmetric. However, the transformed Hamiltonian matrix $T^{-1}HT$ is symmetric if the elements of the T matrix are given by [17]

$$T_{jk}=\sqrt{\frac{2}{h_j+\bar{h}_j}}\delta_{jk}. \tag{6}$$

The inverse transformation matrix T^{-1} is used on the eigenvectors of $T^{-1}HT$ to recover the eigenvectors of the original H matrix.

III. WAVE PACKET STUDIES ON A MODEL ATOM

A numerical representation of the time-dependent Schrödinger equation for two electrons moving in the field of a nucleus may be derived from a simple extension of the variational form found in Eq. (1). To explore various choices for a continually changing nonuniform mesh, we first examine three-body Coulomb scattering using an s-wave model developed by Temkin [18] and Poet [19]. The radial Hamiltonian is given by

$$H=-\frac{1}{2}\frac{\partial^2}{\partial r_1^2}-\frac{1}{2}\frac{\partial^2}{\partial r_2^2}-\frac{Z}{r_1}-\frac{Z}{r_2}+\frac{1}{r_>}, \tag{7}$$

where $r_>=\max(r_1,r_2)$. The time-dependent radial wave function satisfies the initial condition

$$P_{ss}(r_1,r_2,t=0)=P_{1s}(r_1)g_{ks}(r_2), \tag{8}$$

where $P_{1s}(r)$ is the ground-state radial orbital of He^+ and the incoming electron wave packet $g_{ks}(r)$ is a Gaussian of the form

$$g_{ks}(r)=\frac{1}{(w^2\pi)^{1/4}}e^{-(r-r_0)^2/2w^2}e^{-ikr}. \tag{9}$$

In Eq. (9) r_0 is the initial location of the wave packet center, w is the wave packet width, and k is the linear momentum of the incident electron. Spatial discretization of the two kinetic energy operators is the same as found in Eq. (4), while the potential energy operators are represented by diagonal matrices.

We first examine a mesh whose lattice spacing is doubled at specified intervals. To test the general accuracy of this doubling mesh for our time-dependent calculations, we ex-

amine electron scattering on a model He^+ atom using the doubling mesh and then compare it to the scattering system calculated on a fixed mesh. The calculations are performed on a two-dimensional grid where each radial direction spans 48 a.u. An electron wave packet, centered initially at $r_0 = 24$ a.u., travels inwards with an energy of 100 eV along the r_2 axis while interacting with a bound $1s$ electron defined along the r_1 axis. The propagation of the probability density $|P_{ss}(r_1,r_2,t)|^2$ is shown in Fig. 1 for early times during the scattering. In the top row of Fig. 1 are probability density plots using a fixed mesh, while the bottom row is with the doubling mesh. The lattice spacing for both meshes starts at 0.10 a.u., but the spacing for the doubling mesh is increased to 0.20 a.u. at $r_1 = r_2 = 24$ a.u. At $t = 3.6$ a.u., some of the wave function for the doubling mesh has been reflected at the boundary where the lattice spacing is doubled. The reflected piece can be seen moving towards large r_2 at $t = 5.4$ a.u., while the rest of the wave function propagates inward as in the fixed mesh example. This unphysical scattering leads to inaccuracies in the long-time scattering wave function and the resultant cross sections.

In order to avoid reflection, a continuously changing mesh is used for which the lattice spacing is gradually increased at each point. Reflections are avoided due to the small variations in the lattice spacing, yet the ability to cover large radial distances is retained since the lattice spacing is continually being increased. The example used above for the doubling mesh was repeated with this continuously changing mesh where the lattice spacing starts at 0.10 a.u., but is increased by 0.001 a.u. at each subsequent point. This mesh requires only 226 points for each radial direction, compared to 480 needed with a fixed mesh, and yields results that agree very well with the fixed mesh results. A plot of the probability density of the variable mesh results in the form of Fig. 1 is indistinguishable from the fixed mesh plots.

IV. TIME-DEPENDENT CLOSE-COUPLING FOR He^+

We now use the continuously changing mesh to perform full time-dependent close-coupling calculations for electron scattering from He^+. The total Hamiltonian is given by

$$H = -\frac{1}{2}\nabla_1^2 - \frac{1}{2}\nabla_2^2 - \frac{Z}{r_1} - \frac{Z}{r_2} + \frac{1}{|\vec{r_1} - \vec{r_2}|}. \tag{10}$$

The time-dependent wave function for a particular LS symmetry has the form

$$\psi^{LS}(\vec{r_1},\vec{r_2},t) = \sum_{\ell_1\ell_2} \frac{P^{LS}_{\ell_1\ell_2}(r_1,r_2,t)}{r_1 r_2} W^L_{\ell_1\ell_2}(\hat{r_1},\hat{r_2}), \tag{11}$$

where

$$W^L_{\ell_1\ell_2}(\hat{r_1},\hat{r_2}) = \sum_{m_1 m_2} C^{\ell_1\ell_2 L}_{m_1 m_2 0} Y_{\ell_1 m_1}(\hat{r_1}) Y_{\ell_2 m_2}(\hat{r_2}). \tag{12}$$

The time-dependent radial wave functions satisfy the initial condition

$$P^{LS}_{\ell_1\ell_2}(r_1,r_2,t=0) = \sqrt{\tfrac{1}{2}}[P_{1s}(r_1)\delta_{\ell_1,0} g_{k\ell_2}(r_2) + (-1)^S g_{k\ell_1}(r_1) P_{1s}(r_2)\delta_{\ell_2,0}], \tag{13}$$

and the incoming electron wave packet $g_{k\ell}(r)$ is a Gaussian of the form

$$g_{k\ell}(r) = \frac{1}{(w^2\pi)^{1/4}} e^{-(r-r_0)^2/2w^2} e^{-ikr} e^{i\pi\ell/2}. \tag{14}$$

Spatial discretization of the radial parts of the two kinetic energy operators is the same as found in Eq. (4), while the angular and electrostatic potential energy operators are represented by diagonal matrices.

To gauge the strength of the high-order perturbative effects in the TDCC lattice calculations, we also carried out first-order perturbative distorted-wave calculations for electron scattering from He^+. The LS term specific angular algebra for both excitation and ionization is obtained from a modified version of the WEIGHTS program of Scott and Hibbert [20]. The distorted-wave potentials are the configuration-average Hartree potentials for the direct interaction and a local density approximation for the exchange interaction. The LS distorted-wave programs have been used recently to calculate excitation and ionization cross sections for neutral Li [6,21]. Besides providing first-order perturbative excitation and ionization cross sections, the distorted-wave method is also used to ''top-up'' the nonperturbative TDCC calculations by providing high partial wave contributions up to $L = 50$.

Applying the TDCC method to e-He^+ scattering, we choose a 480×480 point grid. The lattice spacing, initially 0.10 a.u., is increased by 0.001 at each point up to a maximum value of 0.40 a.u. and held constant afterward. With this mesh each radial direction extends to about $R = 150$ a.u. and supports spectroscopic He^+ orbitals up to $n = 10$. The results are then compared to a fixed mesh calculation, also on a 480×480 point grid, with a constant lattice spacing of 0.10 a.u. so that R extends to 48 a.u. This mesh can only support spectroscopic He^+ orbitals up to $n = 4$.

The TDCC calculations are performed at electron impact energies of 100, 200, and 300 eV for $L = 0$ to $L = 6$. Each LS symmetry includes enough l_1, l_2 pairs to achieve convergence; four pairs for $L = 0$ up to 23 pairs for $L = 6$. The initial wave function, Eq. (13), is propagated in time, using Eq. (5) for a sufficient time so that wave function moves inwards and then outwards from the origin. The probability of excitation as a function of time for $1s \rightarrow n\ell$ is calculated by using [3]

$$\wp_{n\ell}^{LS}(t)=2\sum_{\ell'}\ \delta(\ell\ell' L)\left\{\int_0^\infty dr_2\left[\int_0^\infty dr_1 P_{\ell\ell'}^{LS}(r_1,r_2,t)P_{n\ell}(r_1)\right]^2-\sum_{n'\ell'}\left[\int_0^\infty dr_2\int_0^\infty dr_1 P_{\ell\ell'}^{LS}(r_1,r_2,t)P_{n\ell}(r_1)P_{n'\ell'}(r_2)\right]^2\right\}, \tag{15}$$

where $\delta(\ell_1\ell_2\ell_3)$ is a triangle identity and $P_{n\ell}(r)$ are the bound orbitals obtained by diagonalization of the Hamiltonian represented on the 480-point mesh as outlined in Sec. II. The wave function is propagated for time $t=T$, until all the excitation probabilites are converged to a constant value. Once the final excitation probability is found, the excitation cross can be obtained by using

$$\sigma(1s\rightarrow n\ell)=\frac{\pi}{4k^2}\sum_L\ \sum_S\ (2L+1)(2S+1)\wp_{n\ell}^{LS}(t=T). \tag{16}$$

The final ionization probability is given by

$$\wp_{ion}^{LS}=1-\sum_{n\ell}\ \wp_{n\ell}^{LS}(t=T)-\sum_{n\ell}\ \sum_{n'\ell'}\left[\int_0^\infty dr_2\int_0^\infty dr_1 P_{\ell\ell'}^{LS}(r_1,r_2,t=T)P_{n\ell}(r_1)P_{n'\ell'}(r_2)\right]^2 \tag{17}$$

and the ionization cross section is

$$\sigma_{ion}=\frac{\pi}{4k^2}\sum_L\ \sum_S\ (2L+1)(2S+1)\wp_{ion}^{LS}. \tag{18}$$

The resulting ionization and excitation cross sections are topped up for $L>6$ with perturbative distorted-wave calculations.

Total electron-impact ionization cross sections for He^+, using the variable mesh TDCC method, are compared with the experimental measurements and distorted-wave and the convergent close-coupling theory in Fig. 2. The variable mesh TDCC results are represented by filled squares, the convergent close-coupling results [13] are displayed as a dot-dash line, the dotted line is our distorted-wave results, and the circles represent experimental measurements obtained by Peart *et al.* [11]. The experimental points at 200 and 300 eV have been shifted slightly to avoid overlapping with the time-dependent points. While the experiment, the time-dependent close-coupling theory, and the convergent close-coupling theory all agree to each other within 6%, the distorted-wave curve lies about 10% higher at the peak than the rest of the results. Time-dependent results on a fixed mesh are not shown in the figure since they agree quite well with the variable mesh results. Measurements taken by Defrance *et al.* [12] are in close agreement with Peart *et al.* [13] and the *R*-matrix *B*-spline calculations performed by van der Hart [14] agree well with the other nonperturbative theoretical methods.

The variable mesh allows us to calculate excitation cross sections to higher n states than with the fixed mesh. Excitation cross sections for $1s\rightarrow ns,np$ for $n=2$ to $n=9$ are shown in Figs. 3 and 4. The filled squares represent variable mesh TDCC results, the dot-dash line again represents convergent close-coupling, and the dashed line is the distorted-wave results. If plotted, the fixed mesh TDCC excitation

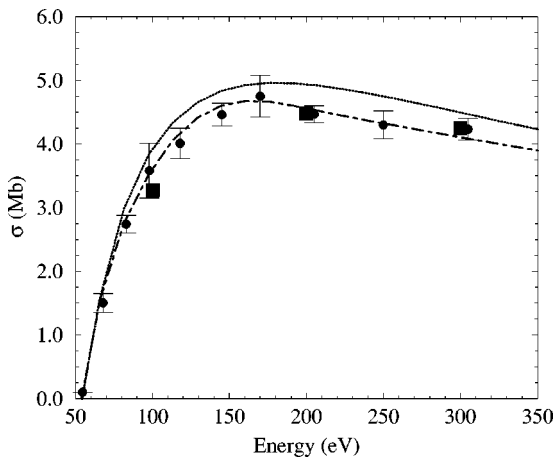

FIG. 2. Total ionization cross section for e-He^+ scattering. Filled squares, time-dependent close-coupling theory with variable mesh; filled circles, experiment [11]; dot-dash curve, convergent close-coupling theory [13]; dotted curve, distorted-wave theory ($1\ \mathrm{Mb}=10^{-18}\ \mathrm{cm}^2$).

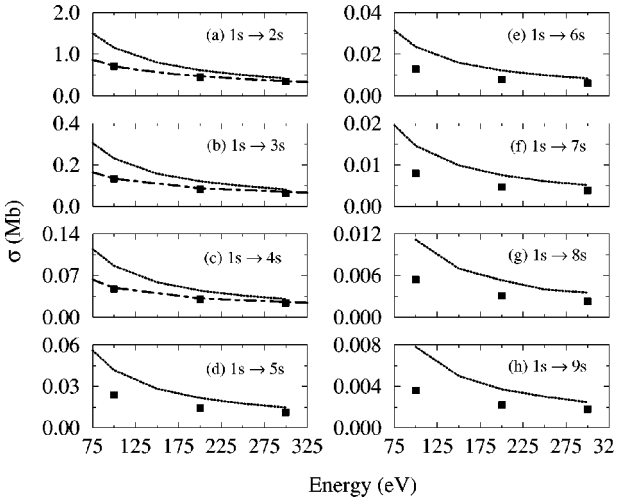

FIG. 3. Excitation cross sections for $1s\rightarrow ns$ for $n=2$ to 9 ($1\ \mathrm{Mb}=10^{-18}\ \mathrm{cm}^2$). Filled squares, time-dependent close-coupling theory with variable mesh; dot-dash curve, convergent close-coupling theory [15]; dotted curve, distorted-wave theory.

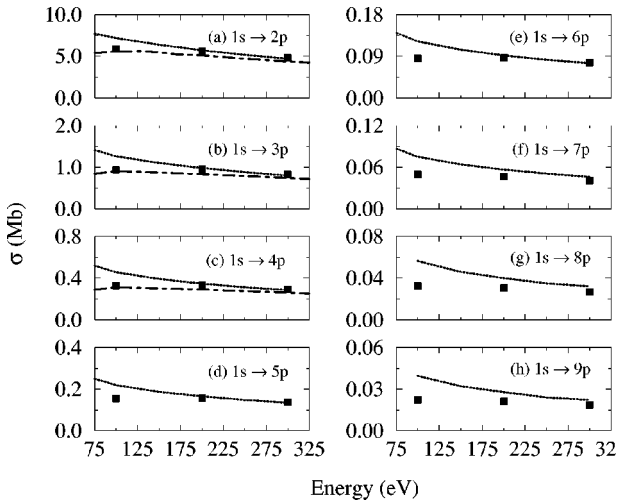

FIG. 4. Excitation cross sections for $1s \rightarrow np$ for $n=2$ to 9 (1 Mb$=10^{-18}$ cm^2). Filled squares, time-dependent close-coupling theory with variable mesh; dot-dash curve, convergent close-coupling theory [15]; dotted curve, distorted-wave theory.

cross sections for $n=2$ to $n=4$ would overlap the variable mesh points. There is also excellent agreement between the time-dependent and convergent close-coupling transitions [15] up to $1s \rightarrow 4s,4p$ after which no convergent close-coupling data is available. The *R*-matrix pseudostate calculations [22] with an incident electron energy of 100 eV have been performed for $1s \rightarrow 2s$ and up to $1s \rightarrow 4p$ and agree well with our variable mesh TDCC calculations. The variable mesh time-dependent data is consistently lower than the distorted-wave results and the relative difference tends to increase with *n*. This trend is shown in Fig. 5, where the percent difference between the distorted-wave and the time dependent cross sections at an incident energy of 100 eV is plotted versus *n* for $1s \rightarrow ns,np$.

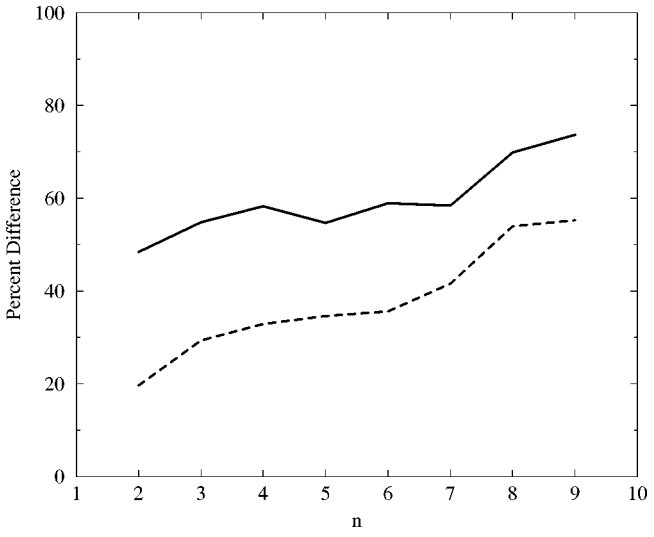

FIG. 5. Percent relative difference between time-dependent close-coupling and distorted-wave excitation cross sections vs principal quantum number *n* of final state for an incident electron energy of 100 eV. Solid curve, $1s \rightarrow ns$; dashed curve, $1s \rightarrow np$.

The small difference between the TDCC cross sections for the variable and fixed meshes depends on many factors. When constructing the fixed mesh grid, the lattice spacing and box size determine the accuracy of the calculation. Accuracy using a variable mesh is more complicated. Care must be taken when choosing the mesh spacing increment and the maximum mesh spacing as well as the initial mesh spacing and the box size. In general, as the mesh spacing increment for the variable mesh increases, the resulting cross sections differ more from the fixed mesh cross sections. This difference is partially offset, however, at large total angular momentum since the larger box size obtained with the variable mesh represents the high partial waves more accurately. The difference between the fixed mesh and variable mesh excitation cross sections for $n=2$ to $n=4$ resulting from any of the above factors is typically within 5% for the variable mesh parameters used in these calculations. The excitation cross sections for large *n* presented in this paper are probably less accurate than for low *n*, but we believe they are still accurate within 10%. We note that the differences between the variable mesh and fixed mesh calculations for cross sections summed over the angular momentum in an *n* manifold, and also for the total ionization cross section, are generally within 5%.

V. SUMMARY

The formulation of the time-dependent close-coupling method is extended to include variable lattice spacings. The size of the numerical region in which the Coulomb interactions between two electrons and a positive atomic core are treated exactly is substantially increased without a concurrent increase in the overall computational run time. Therefore, the strong correlation effects found in the electron ionization of atoms near threshold, and in the electron excitation of atoms to high *n* bound states, are more easily investigated. We find that the TDCC variable mesh results calculated for electron impact energies of 100, 200, and 300 eV agree within 6% of the experimental measurements and the converged close-coupling calculations for the electron-impact ionization of He^+. Of equal importance, the TDCC variable mesh method allows us to calculate $1s \rightarrow nl$ excitations of He^+ to *n* values well beyond the reach of the experiment and the previous nonperturbative theory.

Populations of various species in a plasma can be calculated by using collisional-radiative modeling [23], which requires reaction rates for many collisional and radiative processes including electron-impact excitation from the ground state. Recent collisional-radiative modeling efforts [24] have included nonperturbative calculations for collisional excitation processes from ground up to $n=5$, and scale those excitation rates as n^3 for larger *n*. The TDCC method with variable lattice spacings allows us to check other nonperturbative calculations up to $n=5$. For those systems where there are substantial differences between the nonperturbative and perturbative calculations for excitations up to $n=5$, as in He^+, we find that those differences may even grow larger for higher *n*. Thus, in those systems, the use of perturbative

methods for excitation from the ground to any excited state may be quite inaccurate.

ACKNOWLEDGMENTS

We wish to thank Professor Francis Robicheaux, Professor Ken Schafer, and Professor Don Griffin for useful discussions. This work was supported in part by the U.S. Department of Energy through a grant for theoretical research in plasma and fusion science and a grant for scientific discovery through advanced computing, both administered through Auburn University. Computational work was carried out at the National Energy Research Scientific Computing Center in Oakland, California.

[1] I. Bray and A.T. Stelbovics, Phys. Rev. Lett. **70**, 746 (1993).
[2] D. Kato and S. Watanabe, Phys. Rev. Lett. **74**, 2443 (1995).
[3] M.S. Pindzola and F.J. Robicheaux, Phys. Rev. A **54**, 2142 (1996).
[4] K. Bartschat and I. Bray, J. Phys. B **29**, L577 (1996).
[5] M. Baertschy, T.N. Rescigno, W.A. Isaacs, X. Li, and C.W. McCurdy, Phys. Rev. A **63**, 022712 (2001).
[6] D.C. Griffin, D.M. Mitnik, J. Colgan, and M.S. Pindzola, Phys. Rev. A **64**, 032718 (2001).
[7] K. Bartschat and I. Bray, J. Phys. B **30**, L109 (1997).
[8] P.J. Marchalant, K. Bartschat, and I. Bray, J. Phys. B **30**, L435 (1997).
[9] D.C. Griffin, N.R. Badnell, and M.S. Pindzola, J. Phys. B **33**, 1013 (2000).
[10] F. Herman and S. Skillman, *Atomic Structure Calculation* (Prentice-Hall, Englewood Cliffs, NJ, 1963).
[11] B. Peart, D.S. Walton, and K.T. Dolder, J. Phys. B: At. Mol. Opt. Phys. **2**, 1347 (1969).
[12] P. Defrance, F. Brouillard, W. Claeys, and G. Van Wassenhove, J. Phys. B **14**, 103 (1981).
[13] I. Bray, I.E. McCarthy, J. Wigley, and A.T. Stelbovics, J. Phys. B **26**, L831 (1993).
[14] H.W. van der Hart, J. Phys. B **34**, L147 (2001).
[15] I. Bray (private communication).
[16] S.L. Adler and T. Piran, Rev. Mod. Phys. **56**, 1 (1984).
[17] M.S. Pindzola, T.W. Gorczyca, and C. Bottcher, Phys. Rev. A **47**, 4982 (1993).
[18] A. Temkin, Phys. Rev. **126**, 130 (1962).
[19] R. Poet, J. Phys. B: At. Mol. Opt. Phys. **11**, 3081 (1978).
[20] N.S. Scott and A. Hibbert, Comput. Phys. Commun. **28**, 189 (1982).
[21] J. Colgan, M.S. Pindzola, D.M. Mitnik, D.C. Griffin, and I. Bray, Phys. Rev. Lett. **87**, 213201 (2001).
[22] C. Ballance (private communication).
[23] A. Burgess and H.P. Summers, Mon. Not. R. Astron. Soc. **174**, 345 (1976).
[24] H. Anderson, M.G. von Hellermann, R. Hoekstra, L.D. Horton, A.C. Howman, R.W.T. Konig, R. Martin, R.E. Olson, and H.P. Summers, Plasma Phys. Controlled Fusion **42**, 781 (2000).